

A statistical shape model for radiation-free assessment and classification of craniosynostosis

Matthias Schaufelberger¹, Reinald Peter Kühle³, Andreas Wachter¹, Frederic Weichel³, Niclas Hagen², Friedemann Ringwald², Urs Eisenmann², Jürgen Hoffmann³, Michael Engel³, Christian Freudlsperger³, and Werner Nahm¹

¹Institute of Biomedical Engineering (IBT), Karlsruhe Institute of Technology (KIT), Kaiserstr. 12, 76137 Karlsruhe, Germany

²Institute of Medical Informatics, Heidelberg University Hospital, Im Neuenheimer Feld 130.3, Heidelberg, Germany

³Department of Oral, Dental and Maxillofacial Diseases, Heidelberg University Hospital, Im Neuenheimer Feld 400, Heidelberg, Germany

March 29, 2022

Abstract

The assessment of craniofacial deformities requires patient data which is sparsely available. Statistical shape models provide realistic and synthetic data enabling comparisons of existing methods on a common dataset.

We build the first publicly available statistical 3D head model of craniosynostosis patients and the first model focusing on infants younger than 1.5 years. We further present a shape-model-based classification pipeline to distinguish between three different classes of craniosynostosis and a control group on photogrammetric surface scans. To the best of our knowledge, our study uses the largest dataset of craniosynostosis patients in a classification study for craniosynostosis and statistical shape modeling to date.

We demonstrate that our shape model performs similar to other statistical shape models of the human head. Craniosynostosis-specific pathologies are represented in the first eigenmodes of the model. Regarding the automatic classification of craniosynostosis, our classification approach yields an accuracy of 97.8%, comparable to other state-of-the-art methods using both computed tomography scans and stereophotogrammetry.

Our publicly available, craniosynostosis-specific statistical shape model enables the assessment of craniosynostosis on realistic and synthetic data. We further present a state-of-the-art shape-model-based classification approach for a radiation-free diagnosis of craniosynostosis.

1 Introduction

1.1 Craniosynostosis

Craniosynostosis is characterized by the premature fusion of skull sutures in infants and results in irregular growth patterns. The reported prevalence is three to six cases per 10,000 live births [1, 2, 3]. Craniosynostosis can occur isolated (affecting one suture) or non-isolated (affecting multiple sutures). Syndromic conditions such as Crouzon, Muenke, or Pfeiffer syndrome have genetic reasons and lead to multi-suture synostosis. These syndromes tend to show phenotypical craniofacial findings. Unlike syndromic cases, the causes of isolated craniosynostosis are believed to be multifactorial. Hereditary conditions and genetic mutations have been identified to cause premature fusion of specific sutures [4]. Symptoms of isolated craniosynostosis are a deformity of the neurocranium and consecutively viscerocranium. Craniosynostosis has been linked to elevated intracranial pressure [5] which can lead to reduced brain growth and reduced neuropsychological development [6]. Depending on the involved suture, isolated craniosynostosis can be distinguished into sagittal synostosis (scaphocephaly), metopic synostosis (trigonocephaly), unilateral coronary synostosis (anterior plagiocephaly), lambda synostosis (posterior plagiocephaly) and bicoronal synostosis (brachycephaly). Although brachycephaly includes the synostosis of both coronal sutures, the medical community counts it among isolated synostosis. Surgical treatment involves resection of the synostosis as well as remodeling and reshaping of the cranial vault. The operation aims to prevent abnormal brain growth, thus enabling a regular development of skull and face [7, 8]. Complications during surgery are rare [9] and in most cases a normalized head shape is achieved [10]. The most important differential diagnosis for craniosynostosis are head deformities caused by positioning without suture fusion. These head deformities most commonly present as a non-synostotic posterior plagiocephaly. Positioning deformities are often treated with positioning pillows, helmet therapy or changes in positioning behavior [11]. For further reading, the reader is referred to [12].

As determined by Virchow’s Law, the premature closure of a suture limits the expansion of the skull perpendicular to the fused suture and causes compensatory growth along the suture, resulting in distinct head shapes [13]. During diagnosis, physicians perform visual examination, palpation, cephalometric measurements, and medical imaging. Computed tomography (CT) imaging is the gold standard for diagnostic imaging as well as surgical planning and is routinely performed in many craniofacial centers worldwide. However, this exposes infants to ionizing radiation which should be avoided [8]. One alternative imaging method is Black Bone magnet resonance imaging [14, 15], which has the notable drawbacks that during image acquisition, infants are required to be sedated to prevent them from moving. Sonographic examinations and 3D photogrammetry are radiation-free and broadly available diagnostic options. Photogrammetric scans provide inexpensive and fast means to objectively quantify head shape without exposure to radiation nor the need of sedation. They are often used to monitor the condition before surgery and the head development after the operation [16].

1.2 Statistical shape modeling

Statistical shape modeling describes the approach to capture variations of geometric shapes by statistical methods. In the medical field, applications of statistical shape models (SSMs) include distinguishing pathological from physiological subjects, assisting in surgical planning, or shape classification. Point distribution models (PDMs) are the most common type of SSMs and use a point cloud representation. [17] introduced the idea to construct PDMs using training instances. A key requirement of this approach is that point identifiers across training instances share the same

morphological meaning. Landmarks are such points, but are often only sparsely available, so intermediate points must be included to obtain a full model. Accurate correspondence establishment is crucial and has a high influence on the model performance, but is at the same time difficult to evaluate as no ground truth is available. After dense correspondence establishment, a statistical analysis is performed by computing sample mean and sample covariance matrix of the training data. Usually, this is a principal component analysis (PCA) or a variation of it which is applied on the covariance matrix, arranging the principal components according to their respective variance in the training data. Synthetic, valid shapes are constructed by linear combinations in the vector space defined by the principal components and constrained by their respective eigenvalues.

Shape models of the human face have become popular types of PDMs. Some of the most important publicly available shape models of the human face are the Basel Face Model [18, 19] and the Large Scale Facial Model [20]. The Liverpool-York-Head-Model is the first publicly available shape model of the full human head in both shape and texture [21] and includes a child model constructed from subjects between 2 and 15 years. [22] gives a overview about face models, current trends, applications, and challenges.

1.3 Assessment and classification of head deformities using shape analysis

Researchers studied anatomic differences between physiological subjects and patients with craniosynostosis [23] as well as therapy outcome [24] using CT scans on both 2D and 3D approaches. [25] discriminated between scaphocephaly and control subjects using a support vector machine (SVM) on the sampled 2D contour of the skull on the axial plane of CT scans. [26] performed a statistical analysis on CT scans of physiological subjects before comparing them to subjects of scaphocephaly. [27] developed a shape analysis framework for the quantification of diagnostic features of CT scans. In their follow-up publication [28], they proposed a classification framework to distinguish between types of craniosynostosis using shape descriptors from an SSM and fusion indices of the ossified sutures extracted from CT scans. They also performed a classification using linear discriminant analysis (LDA) and an SVM on 141 cases, the majority being physiological subjects with an overall accuracy of 95.7% using a leave-one-out classifier.

Recently, the use of radiation-free 3D stereophotographs for head shape assessment and classification of craniosynostosis gained momentum. [29] proposed a 2D SSM of craniofacial profile and evaluated contour changes after surgical intervention of 25 craniosynostosis patients. [30] evaluated surgical spring-assisted therapy by using the principal components of an SSM to assess surgical parameters. [31] constructed a PDM by determining the intersections of cast rays onto photogrammetric scans of 100 patients and found statistically significant differences between the control group and both scaphocephaly and trigonocephaly patients. Regarding the classification of craniosynostosis, [32] proposed a dense neural network to classify different types of craniosynostosis using ray casting to compute the distances between a center point and the surface of 3D stereophotographs of the head. Using stratified 10-fold cross validation on 196 subjects, they correctly classified 99.5% of their subjects.

1.4 Scope of this work

Works of previous authors using SSMs from 3D surface scans showed promising first results to distinguish features of different head deformities [31, 30, 33]. However, no craniosynostosis-specific SSM has been made publicly available, so methods are tested on in-house datasets making quan-

titative comparisons between methods difficult. Existing publicly available SSMs are trained on healthy adults and children [21], thus assessing head deformities in terms of healthy, physiological variations of head shapes.

An SSM of infants with and without head deformities can be used to create a dataset which serves as a baseline for comparison studies for pathological features, for classification studies, and for mesh manipulation applications such as patient counseling, shape reconstruction or the creation of synthetic data with specific pathological features. Active shape model approaches could use an SSM of craniosynostosis patients for facilitating automated segmentation.

This publication makes the following contributions:

- We propose the first publicly available SSM of craniosynostosis patients using 3D surface scans, including pathology-specific submodels, texture, and 100 synthetic instances of each class. It is the first publicly available model of children younger than 1.5 years and SSM of craniosynostosis patients including both full head and texture. Our model is compatible with the Liverpool-York head model [34] as it makes use of the same point identifiers for correspondence establishment. This enables combining texture and shape of both models.
- We present an alternative classification approach directly on the parameter vector of our SSM composed of 3D photogrammetric surface scans. We test five different classifiers on our database consisting of 367 subjects and achieve state-of-the-art results. To the best of our knowledge, we conduct the largest classification study of craniosynostosis to date.
- We demonstrate two applications of our SSM: First, with regards to patient counseling, we apply attribute regression as proposed by [18] to remove the scaphocephaly head shape of a patient. Second, for pathology specific data augmentation, we use a generalized eigenvalue problem to define fixed points on the cranium and maximize changes on face and ears as proposed by [35]. To the best of our knowledge, neither of these applications have been applied to patients using a craniosynostosis shape model before.

2 Materials and methods

Fig. 1 gives a full overview of the pipeline from the raw data to the SSM creation and the craniosynostosis classification. We describe each of the top-level blocks in detail in the following subsections.

2.1 Dataset and preprocessing

At the Department of Oral, and Maxillofacial Surgery of the Heidelberg University Hospital photogrammetric surface scans are used in the daily routine to diagnose and document patients with craniofacial diseases. In this study we were concerned with patients suffering from craniosynostosis. Out of the scans that were acquired between 2011 and 2020, 367 preoperative 3D photogrammetric scans were extracted. We used a standardized protocol, which had been examined and approved by the Ethics Committee Medical Faculty of the University of Heidelberg (Ethics number S-237/2009). The study was carried out according to the Declaration of Helsinki and written informed consent was obtained from parents. The Canfield VECTRA-360-nine-pod

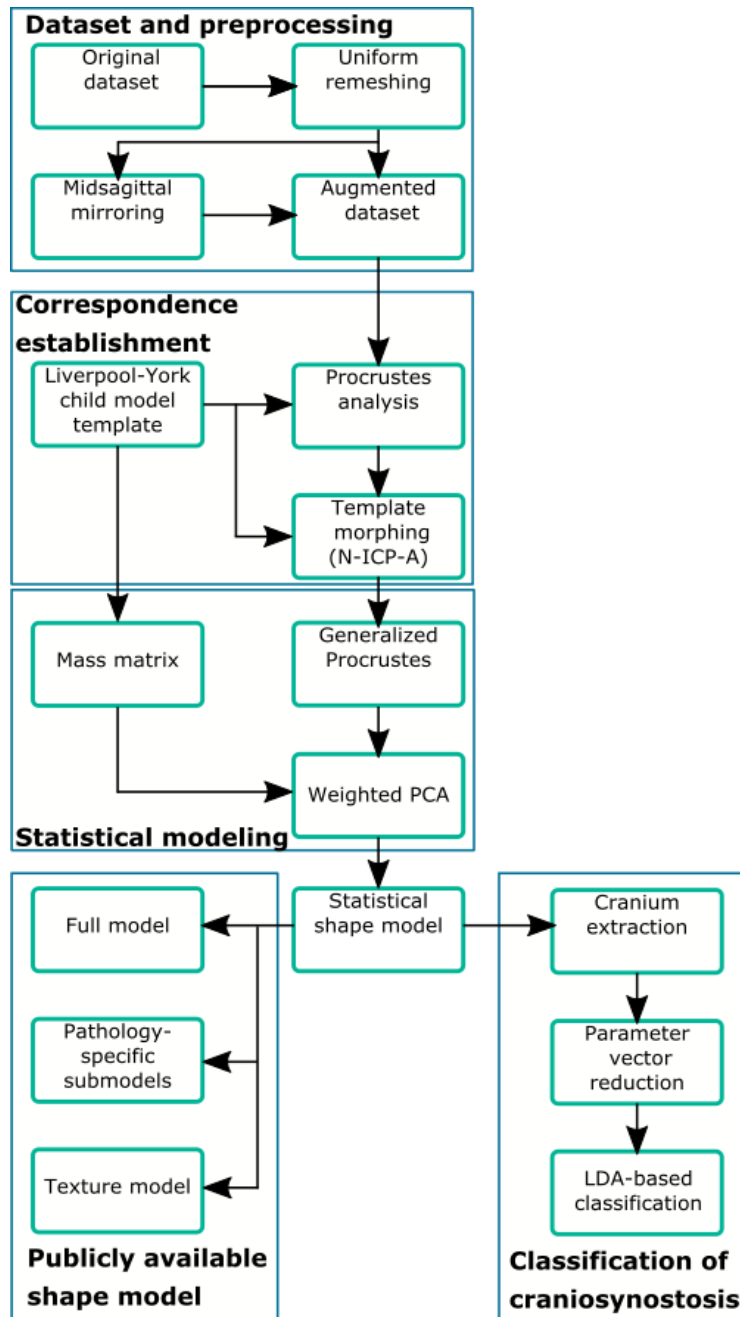


Figure 1: Shape model creation and classification pipeline.

system (Canfield Science, Fairfield, NJ, USA) was used for recording. To avoid artifacts on the head due to hair, the scanned infants wore tight fitting nylon caps. For each of the recordings, the dataset provided the 3D vertex coordinates, UV texture coordinates, and the triangular face indices connecting the vertices to a mesh surface. Each recording contained additional metadata, which includes the medical diagnosis of the physician, the patient’s age on the day of the recording, and 10 cranial and facial landmarks manually annotated by a medical expert. In the appendix, we summarize the aforementioned landmarks in Table 6.

We retrieved patient scans classified with three types of craniosynostosis, namely “coronal suture fusion” (brachycephaly and unilateral anterior plagiocephaly), “sagittal suture fusion” (scaphocephaly), “metopic suture fusion” (trigonocephaly), as well as a control group without any suture fusion. This makes our approach comparable to other classification studies which distinguished between craniosynostosis and non-craniosynostosis classes, in particular [28] and [32]. Besides healthy subjects, our control group contained also scans of children with positional posterior plagiocephaly without suture fusion, who were later treated with helmet therapy or laying repositioning. All craniosynostosis patients later underwent surgical remodeling of the cranium. We show violin plots [36] using a publicly available implementation [37] of the subjects’ age distribution in Fig. 2.

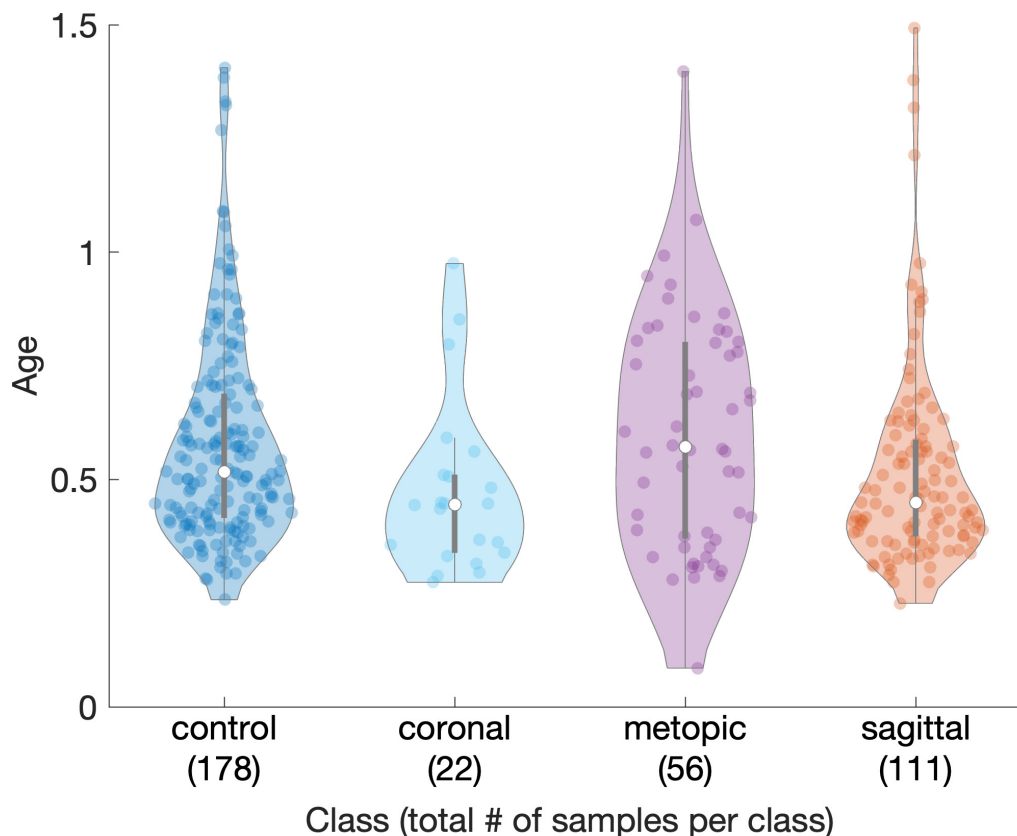


Figure 2: Age distribution among classes of the dataset. Parenthesis indicate number of samples per class.

During recording, the patients had to be held tight, oftentimes the neck of the patient was covered by clothes or the hands of the medical staff. For this reason, some recordings contained isolated parts and other artifacts. Additionally, close to the ears we often found mesh irregularities such as large edge lengths. The open source tool *Meshlab* (ISTI-CNR, Pisa, Italy) [38] was used to remove isolated parts, duplicated vertices, and to close holes. After artifacts removal we used isotropic explicit remeshing [39] to avoid large edge lengths and to obtain a regular, uniform surface scan.

Depending on the model application, it can be advantageous to use a non-regular mesh (having different resolutions on different parts of the mesh). Cranial parts mostly change smoothly in comparison with facial parts and can thus be expressed with fewer vertices and lower spacial resolution to reduce computational cost.

We used the mean shape of the Liverpool-York child head model [21] as a template for correspondence establishment. This template has the advantage of being symmetric and does not have a head deformity avoiding pathological bias during model creation. To directly include eyes and close the mouth in the model we added additional vertices into the template which enables using the model without an additional eye model. The modified template is compatible with the original model as the order of the vertex identifiers is the same. The final template has $p = 13151$ vertices and a mean edge length of 2.91 mm.

2.2 Correspondence establishment

During correspondence establishment we intended to find corresponding points with the same morphological meaning on the template $\mathbf{X} \in \mathbb{R}^{p \times 3}$ and the target scans. To increase our sample size and avoid a symmetry-bias for asymmetric pathological cases for the coronal model, we mirrored each subject on the midsagittal axis thus increasing the dataset size from $N = 367$ to $2N = 734$. To prepare template morphing, we initially aligned the template to each target using the annotated landmarks. We used Procrustes analysis to obtain a linear transformation consisting of translation, rotation, and isotropic scaling which transformed the original template landmarks onto the corresponding target landmarks. By applying the transformation to the whole set of the template points, we aligned the template mesh to each target scan, ensuring that the facial and cranial regions of the template are close to their morphological counterparts on the target scan. Note that this process only facilitates template morphing and does neither rescale nor change the target scans.

Numerous registration algorithms for 3D surface registration exist and have been tested on medical data [40, 41, 21, 34, 42, 20, 19], many of which can be tailored toward specific applications. We tested and evaluated four different state-of-the-art methods which have been successfully used for template morphing of the full head. Two approaches (Two-step Laplace-Beltrami regularized projection (2S-LBRP), iterative coherent point drift with Laplace-Beltrami regularized projection (ICPD-LBRP)) use a Laplace-Beltrami regularized projection (LBRP) approach while the two other other methods (nonrigid iterative closest points affine (N-ICP-A), and nonrigid iterative closest point translation (N-ICP-T)) use an optimal step nonrigid iterative closest points (OS-N-ICP) approach. After evaluating the four methods and the resulting models, we used N-ICP-A as the final method for our model. We continue with a description of the N-ICP-A method.

The OS-N-ICP methods were presented by [43] who base their work mostly on [42]. The core idea is to use an affine transformation for each point and locally regularize transformations of

connected points. A stiffness term penalizes differences between transformations between adjacent nodes. A distance term controls how close the template vertices are transformed to the target points and a landmark term requires that the landmark points of template and target match each other. All three terms, stiffness term, distance term, and landmark term, are optimized simultaneously using an iterative approach starting with a high stiffness. For each stiffness, a correspondence search is performed and the optimal deformation with respect to the found correspondences is computed. As soon as the transformation changes very little, the stiffness parameter is decreased and repeated for the reduced stiffness until convergence. The mathematical formulas are presented in Appendix A, but for detailed explanations, the reader is referred to [43]. We used an exponential decrease of the stiffness parameter and a small landmark term which was set to zero after 50 iterations. We list all hyperparameters in the appendix in Table 7.

A description of the LBRP-based methods is presented in Appendix B and the detailed evaluation and quantitative comparison of all four methods can be found in Appendix C.

2.3 Statistical modeling

To align the morphed templates, we employed rigid generalized Procrustes analysis (GPA) [17]. GPA iteratively calculates the mean shape of the training data, the deviation of the training data to the calculated mean shape, and aligns the training data accordingly. The Euclidean distance was used as the Procrustes distance metric. This removes the non-shape related attributes translation and rotation from the morphed templates. For this study, we considered scale an attribute of shape because craniosynostosis-related features may depend on the patient’s age and head size. After reshaping each of our morphed templates $\mathbf{X}_i \in \mathbb{R}^{p \times 3}$ into columnvectors $\mathbf{x}_i \in \mathbb{R}^{3p}$, we stacked them horizontally to obtain the observation matrix $\mathbf{X}_{\text{Obs}} \in \mathbb{R}^{3p \times 2N}$. We regarded them as independent observations which served as training data upon which we built our SSM. We computed the mean shape $\bar{\mathbf{x}} \in \mathbb{R}^{3p}$ and by subtracting the mean shape from the observations matrix, we obtained the mean-aligned data matrix which we refer to as zero-mean data matrix:

$$\mathbf{X}_{\text{ObsZM}} = \mathbf{X}_{\text{Obs}} - \bar{\mathbf{x}} \quad (1)$$

PCA is a statistical method to compute the eigenvectors and eigenvalues of the sample covariance matrix of the zero-mean training data. One drawback of performing ordinary PCA is that all points are weighted equally regardless of their morphological importance. Consequently, areas with higher vertex density such as the face of our template are therefore over-represented compared to parts with lower vertex density such as the cranium. As [44] proposed, we can use weighted principal component analysis (WPCA) to counterbalance the influence of the face by using a mass matrix.

We defined the mass matrix $\mathbf{M} \in \mathbb{R}^{p \times p}$, composed of per-vertex weights and per-edge weights in a very similar manner to barycentric cells. The diagonal elements of \mathbf{M} represent the vertex weights. Each vertex weight is defined as the sum of the area of the adjacent faces for which this vertex is the nearest neighbor. Likewise, the non-diagonal elements represent the edge weights and each edge weight is defined as the sum of the area of the adjacent faces for which this edge is the closest edge. To account for the vectorized representation of the observations, the mass matrix is then stretched by factor 3 and nearest-neighbor-interpolated, resulting in $\mathbf{M}_3 \in \mathbb{R}^{3p \times 3p}$. We computed the weighted Gram matrix $\mathbf{G}_W \in \mathbb{R}^{2N \times 2N}$ as

$$\mathbf{G}_W = \mathbf{X}_{\text{ObsZM}}^T \mathbf{M}_3 \mathbf{X}_{\text{ObsZM}} \quad (2)$$

and performed an eigendecomposition of \mathbf{G}_W using

$$\mathbf{G}_W = \mathbf{U}_G \mathbf{\Lambda}_G \mathbf{U}_G^T. \quad (3)$$

We computed the principal components $\mathbf{V} \in \mathbb{R}^{3p \times 2N}$ of the training data as

$$\mathbf{V} = \mathbf{X}_{\text{ObsZM}} \mathbf{U}_G \mathbf{\Lambda}_G^{-\frac{1}{2}}, \quad (4)$$

and the eigenvalues $\mathbf{\Lambda} \in \mathbb{R}^{2N \times 2N}$ of the sample covariance matrix of the training data by re-scaling the eigenvalues of the Gram matrix

$$\mathbf{\Lambda} = \frac{1}{2N - 1} \mathbf{\Lambda}_G. \quad (5)$$

Each observation could then be defined using the principal components and eigenvalues using

$$\mathbf{x} = \bar{\mathbf{x}} + \mathbf{V} \mathbf{\Lambda}^{\frac{1}{2}} \alpha. \quad (6)$$

As the data matrix was centered before, the last eigenvalue will be zero and can be omitted.

We created one full model, four class-specific submodels, and one cranium-only model. The full model was created using the full zero-mean observation matrix. The class-specific submodels used the assigned diagnosis label for each observation. For the classification approach, we built a cranial model and extracted the cranial part of the template to remove possible influences of the face. For each model, GPA was performed individually.

2.4 Classification of craniosynostosis

The classifier was trained to distinguish between the labeled classes and thus between the three different types of craniosynostosis and the control class. The cranium model served as a basis for the classifiers. We extracted the coefficient vector α for each observation from the cranial model which served as an input for the classifiers. Using the coefficient vector as shape descriptors and as a direct input for an SVM has been successfully tested in a different domain [45].

We evaluated five different classifiers: SVM [46], LDA [47], naïve Bayes (NB) [48], bagged decision trees (BDTs) [49], and k-nearest-neighbors (kNN) [50]. All classifiers were implemented using the Python module *scikit-learn* [51] (version 1.0.2), mostly sticking to the default settings. SVMs are binary classifiers that use kernel functions to map the input parameters into a high-dimensional representation which can be separated by hyperplanes. We chose a kernel based on radial basis functions and a multi-class model with 6 one-versus-one binary classifiers. For LDAs, we used a multivariate Gaussian distribution for each class assuming the same covariance matrix for each class. Each prediction is assigned to the class whose mean is the closest in terms of the Mahalanobis distance taking into account the prior probability of each class. NB assumes conditional independence between input variables. Similar to LDA, we used a Gaussian model to distinguish between classes. kNN classification classifies the test sample according to the k closest neighbors. We selected $k = 5$ nearest neighbors in Euclidean space. For tie-breaking we chose the nearest neighbor among the tied classes. BDTs are white-box classification algorithms using a hierarchical, tree-like structure. We used the default implementation for tuning the hyperparameters of the BDTs.

We used stratified 10-fold cross validation on the unmirrored samples. For each split, the test set was only composed of the original, unmirrored samples and the training set was augmented

with the mirrored training samples. This way, each of the samples from the original set was used once for testing without the possibility of cross-over.

PCA orders the principal components according to their variance, so the first principal components describe the overall shape while the last components contain mostly noise. The noise can arise e.g., from incorrect morphing, limited resolution, or acquisition errors during scanning. We aimed to reduce the number of principal components based on the assumption that the parameters responsible for a good classification are concentrated in the first components. We iterated over the first 100 principal components and used the accuracy as a fitness function to select the optimal number of principal components. Finally, four different metrics evaluated the final classifier: Beside overall accuracy, we used g-mean, per-class sensitivity, and per-class specificity.

3 Results

3.1 Morphing and model evaluation

We evaluated each template morphing approach using three metrics: landmark errors, vertex-to-nearest-neighbor distances, and per-class surface normal deviations. Landmark errors provide sparse point-to-point errors on known correspondences. Vertex-to-nearest-neighbor distances evaluate how close the template has been morphed onto the target without taking into account if the nearest neighbor is morphologically correct. What we refer to as “surface normal deviations” has been proposed in [43]: we removed translational and rotational components from the morphed templates and computed surface normal deviations between the morphed templates. This evaluates how well point identifiers have been morphed onto morphologically similar regions across all scans. However, our dataset contained different pathologies, so we also expected shape and surface normal differences among different pathology classes. Hence, we modified this approach and computed surface normal deviations on each pathology class separately before calculating the cumulative mean surface normal deviations. Table 1 shows morphing errors for the N-ICP-A method.

Table 1: Mean error and standard deviation for each morphing method. Boldface shows smallest error for each metric.

Mean landmark error (mm)	Mean vertex-to-nearest-neighbor distance (mm)	Mean surface normals deviations (degree)
6.533 ± 1.796	0.007 ± 0.003	33.488 ± 1.578

For shape model evaluation we used the three metrics compactness, generalization, and specificity [52, 53]. Compactness determines the model’s ability to capture most of the variance with few components, generalization the model’s ability to fit to unknown observations, and specificity the model’s ability to create synthetic instances similar to the training data.

In this section, we only show the results for N-ICP-A, the final morphing method. All morphing methods are compared in Appendix C.

We performed a qualitative evaluation of the shape model eigenmodes and submodel mean shapes on the N-ICP-A-model in Fig. 3. A change of the first eigenmode of the full SSM represented a change primarily in size. For the second mode, we observed an elongated head shape characteristic of sagittal suture fusion. In positive direction, we observed a triangular-shaped fore-

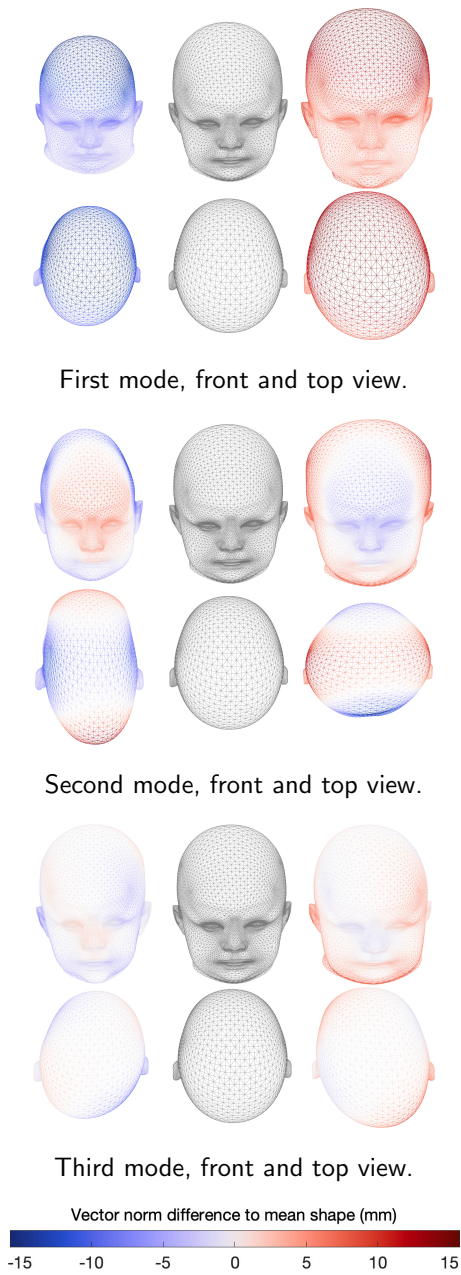


Figure 3: First three modes of the full model in front and top view. From left to right: -3σ , mean shape, and $+3\sigma$. Colorbar indicates vector norm difference between principal component shape and mean shape (gray).

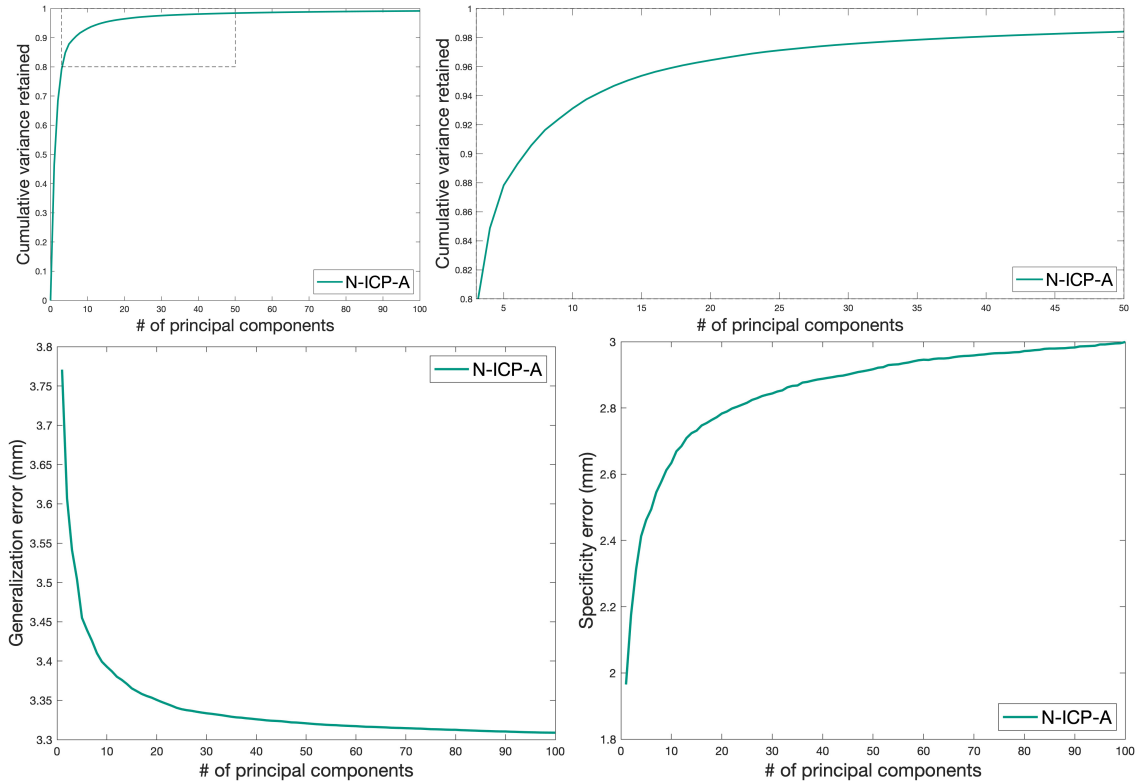


Figure 4: Compactness, generalization, and specificity of the final model as a function of the number of principal components. Top left: Compactness, top right: Zoom-In. Higher is better. Bottom left: Generalization error. Bottom right: Specificity error. Lower is better.

head typically associated with metopic suture fusion. The third direction showed head asymmetry resembling left and right plagiocephaly patients present in the control group.

In Fig. 5 the resulting submodels are evaluated in terms of compactness, generalization, and specificity. However, quantitative comparisons between the submodels are invalid as they differ in sample size. Visually, the mean shapes of each pathological submodel show the typical characteristics of each disease (Fig. 6).

3.2 Publicly available shape model

We provide the N-ICP-A-based SSM, a texture model, triangular mesh mappings, the class-specific submodels, and 100 instances of each model sampled from a Gaussian distribution. The models are publicly available online [?] under the Creative Commons license CC-BY-NC 4.0. For the models, we included 95% – 98% of the total variance. As we used the Liverpool-York child head model as a basis for the initial template for correspondence establishment, the statistical information of both shape and texture of the models can easily be combined. Table 2 provides information on how many components we included in each model.

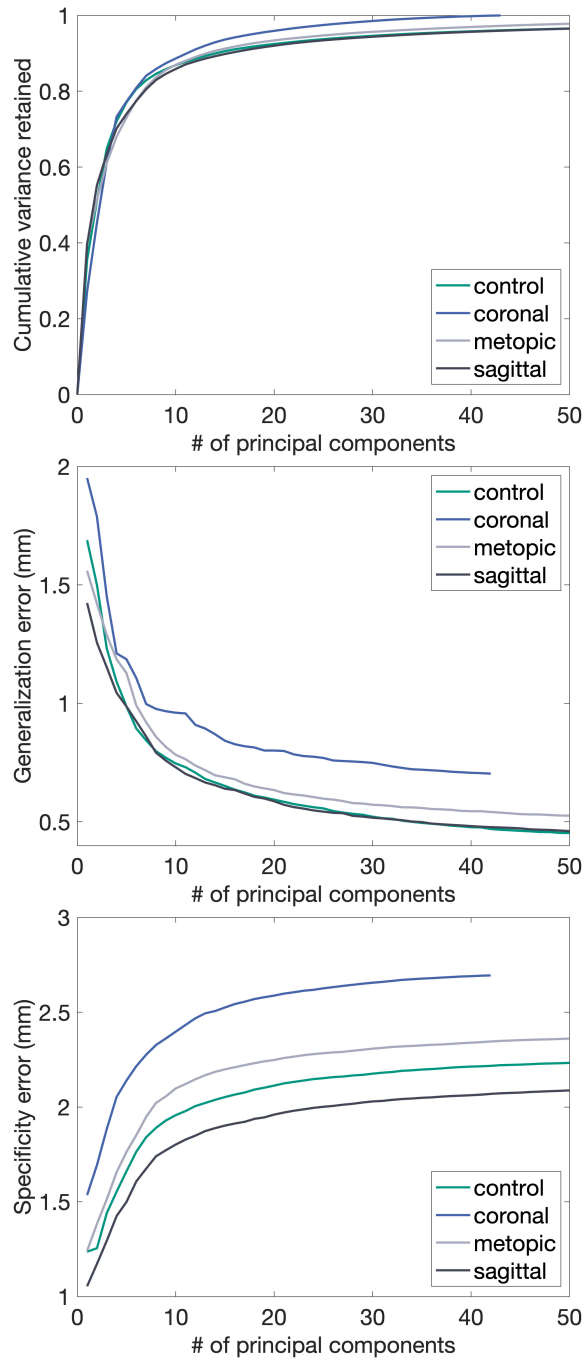


Figure 5: Shape model metrics for the control submodel and the pathology-specific submodels. From left to right: Compactness, generalization, and specificity.

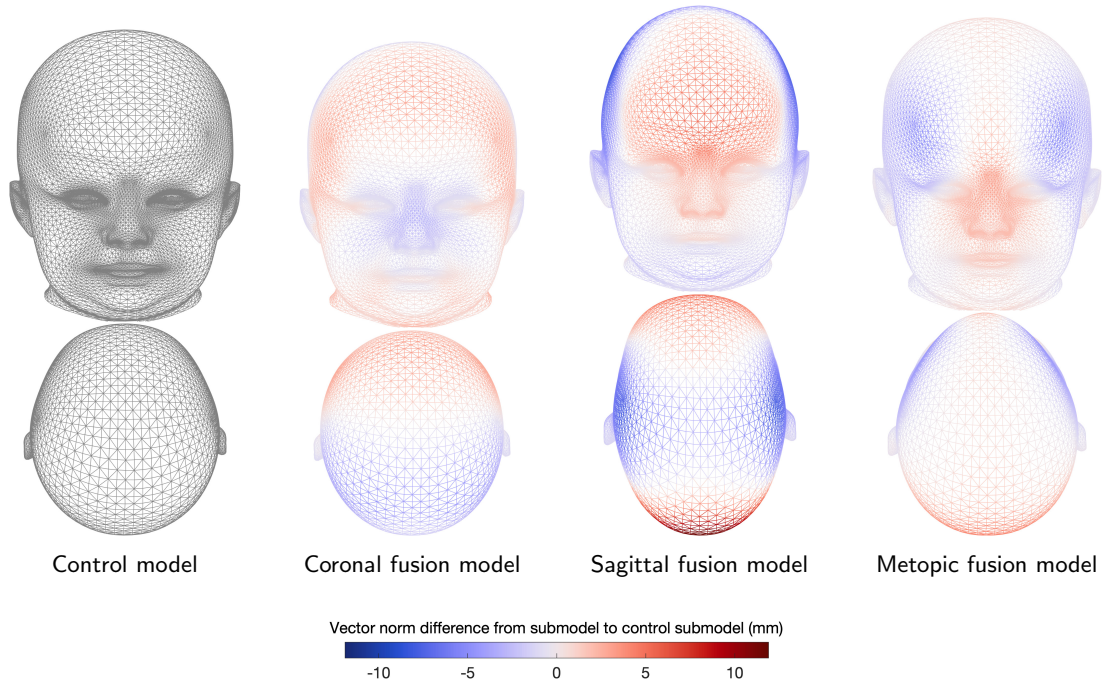


Figure 6: Mean shapes of pathology-specific submodels, front and top view. From left to right: control model, coronal suture fusion model, sagittal suture fusion model, and metopic suture fusion model. Colorbar indicates vector norm difference between principal component shape and mean shape (gray).

3.3 Shape model applications

We illustrate two applications of our SSM. First, we changed the head of a scaphocephaly patient toward the control group. [18] presented an approach to change an attribute (such as gender or weight) using linear regression. As the pathologies in our model can be interpreted as such attributes, we changed the pathology of our samples:

$$\alpha_{\text{ID,control}} = \alpha_{\text{ID}} + \alpha_{\mu,\text{control}} - \alpha_{\mu,\text{sagittal}} \quad (7)$$

We present the resulting pathology change in Fig. 7. This approach can be useful in clinical settings for patient counseling.

Second, we sampled random instances from our shape model while keeping the points on the cranium fixed. Modeling the remaining flexibility on a shape which is held partially fixed can be described as a constrained generalized eigenvalue problem [35]. This approach can be applied to create a synthetic database for machine learning applications and is depicted in Fig. 8. Alternatively, synthetic samples with predefined pathology can also be created using a posterior shape model [54] or by simply using the pathology-specific submodel.

Table 2: Number of principal components included in the publicly available shape model data under Creative Commons license CC-BY-NC 4.0.

Model	Included principal components
Full shape model	100
Texture model	100
Control model	30
Sagittal model	30
Metopic model	25
Coronal model	15

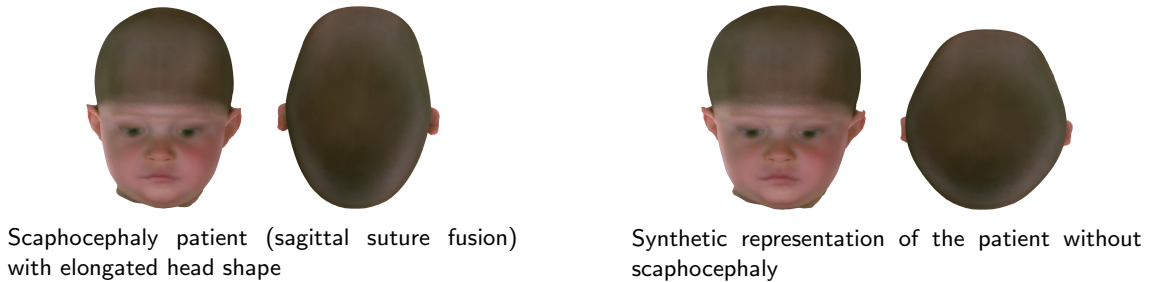


Figure 7: Patient pathology assessment using pathology change. Left: the original head shape of the scaphocephaly patient. Right: the patient’s head with removed pathology using our full SSM.

3.4 Classification results

We tested the five classifiers on the cranial models of each of the four morphing methods. In this section, we only show results for N-ICP-A. A comparison of the classifiers on the other morphing methods can be found in Appendix D. Fig. 9 shows the accuracy over the used number of principal components on the N-ICP-A approach. LDA, SVM, and NB outperformed kNN and BDT. A reduction in accuracy with adding more principal components could be observed for NB and kNN and less pronounced for the SVM.

For the optimal classification setup (LDA with 44 components) we show confusion matrix, per-class sensitivities, per-class specificities, and g-mean in Table 3. The classifier yielded optimal per-class specificities for the pathological cases and the per-class sensitivity for the controls and metopic cases. The remaining per-class sensitivities for the pathological cases were between 0.773 and 0.973 while the per-class specificity for the control group was 0.958. The g-mean resulted in 0.931 and the total accuracy in 0.978.

4 Discussion

We presented the first publicly available craniosynostosis SSM. It unites statistical information of 367 subjects and their mirrored twins with and without craniosynostosis. To date, many methods presented by various authors rely on in-house datasets making quantitative comparisons difficult. A set of synthetic photogrammetric head scans of our SSM can help creating a large patient cohort

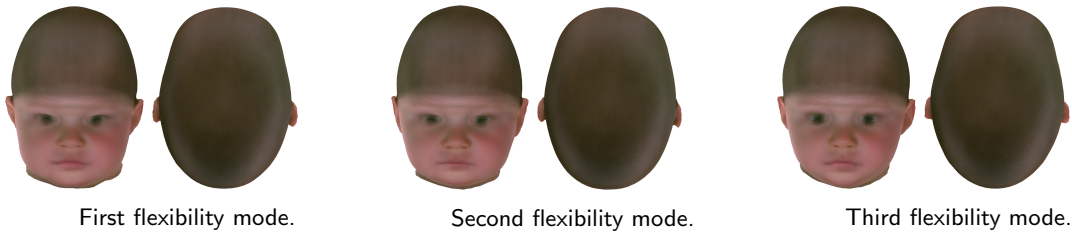


Figure 8: The first three flexibility modes with fixed cranium, applied to a synthetic scaphocephaly patient. Changes are minimal for the cranium and maximal for the face, neck, and ears.

Table 3: Confusion matrix, sensitivity and specificity using linear discriminant analysis (LDA), nonrigid iterative closest points affine (N-ICP-A), and the optimal number of components (44). Con = control, Cor = coronal, Sag = sagittal, Met = metopic.

True class	Predicted class				Sensitivity	Specificity
	Con	Cor	Met	Sag		
Con	178	0	0	0	1.000	0.958
Cor	5	17	0	0	0.773	1.000
Met	0	0	56	0	1.000	1.000
Sag	3	0	0	108	0.973	1.000
G-mean					0.931	
Total accuracy						0.978

for a reproducible evaluation of methods to assess craniosynostosis.

Our model reflects the pathologies available in our dataset: The first two components show changes in size as well as changes related to sagittal and metopic suture fusion. These are the two largest craniosynostosis classes in the dataset. The third principal component is associated with head asymmetry, resulting from non-synostotic positional plagiocephaly subjects in the control class. The pathology-specific submodels also depict the typical head deformities observed in clinical studies and are best used for controlled sampling of labeled synthetic instances.

From the tested template morphing methods, none of the approaches clearly outperformed the other ones. We considered N-ICP-A and ICPD-LBRP to be the two most promising methods. Our decision to use N-ICP-A over ICPD-LBRP for the publicly available model was motivated by the smaller vertex-to-nearest-neighbor-distances and the higher model compactness. Landmark errors are typically considered the gold standard, but as our model is concerned with craniosynostosis and the landmarks are located primarily on the face, we deemed them less important for this model.

A comparison with other craniosynostosis-related SSMs is difficult as we propose the first publicly available model of infants. In the medical field, studies which used shape models [33, 55] did not include quantitative metrics such as landmark error, compactness, generalization, and specificity. Thus, we compare our model to a non-craniosynostosis-related SSMs of the full head. The most comparable SSM might be the Liverpool-York-Model [21, 34], as it is a full head model and also contained a submodel comprising children from 2 to 15 years. Compared with the Liverpool-York head model, our model is more compact, has a lower specificity error, and lower vertex-to-nearest-neighbor distances, but a higher generalization and landmark error. However a

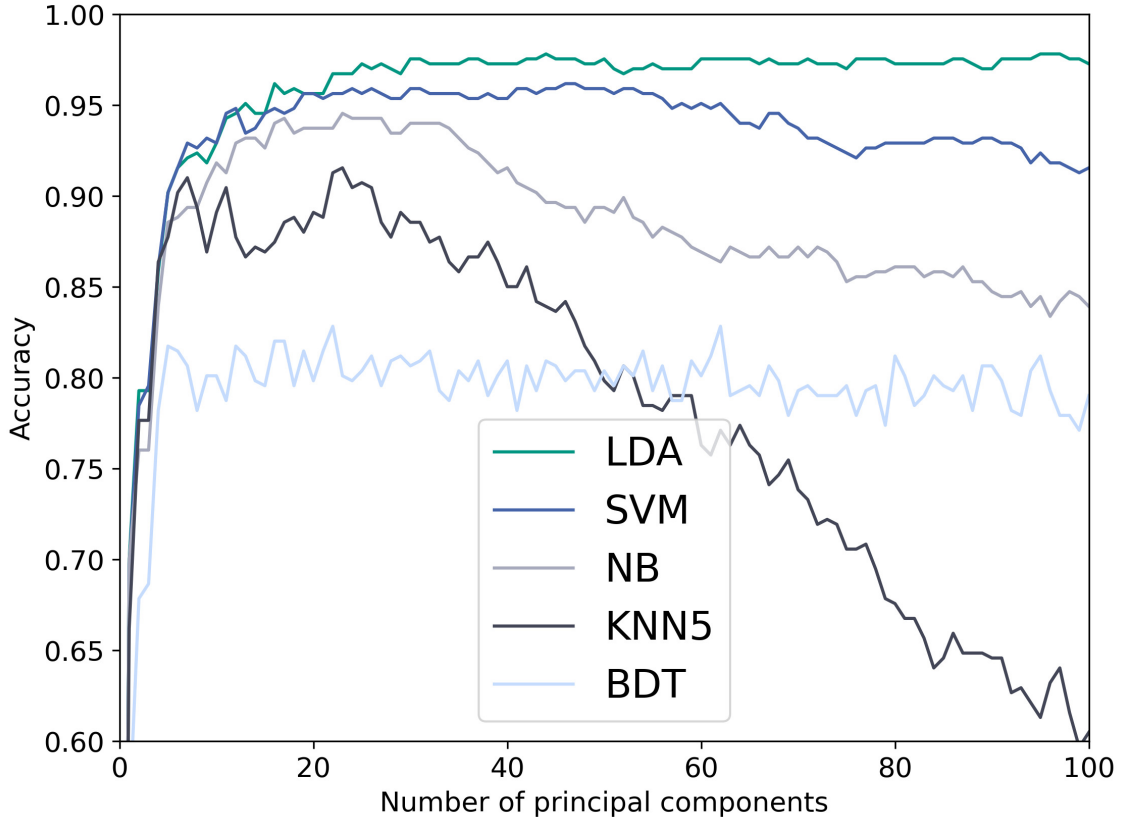


Figure 9: Accuracy as a function of the number of principal components used for the nonrigid iterative closest points affine (N-ICP-A) classifier.

direct comparison may not be meaningful considering that both the dataset and the used mesh resolution are different. Our training data contains only children younger than 1.5 years, so the total variance of our model might be smaller by nature. However, by including a similar LBRP-approach in our analysis, we show that our model performs comparable to state-of-the-art models.

The second contribution of this work is a classification pipeline approach using our SSM. To the best of our knowledge, we tested it on the largest dataset used for a craniosynostosis-related classification study to date. Multiple authors [31, 33] have shown that shape modeling enables a quantitative analysis of the head shape with respect to craniosynostosis. In our work, we demonstrated that SSM can not only quantify, but also classify head deformities. With an accuracy of 97.8% on 367 subjects, our approach classifies craniosynostosis comparable to competing methods: [28] achieved a classification accuracy of 95.7% on 141 subjects using CT data and [32] obtained an accuracy of 99.5% on 196 samples using a feedforward neural network in combination with ray casting and stereophotographs. As each classification approach used different datasets, it can be argued that quantitative comparisons between different approaches might be dataset dependent. However, as we tested multiple classifiers and multiple morphing methods, we demonstrate that our classification approach is robust and does not rely on heavy hyperparameter tuning. Morphing

methods showed little influence in the final classification accuracy. The choice of the classifier had a larger influence on the classification results: LDA and SVM appeared to be the most robust classifier with respect to the noisy components, while NB worked well with fewer than 40 components.

The control class of our study is assembled by the scans of children who visited the hospital without indication to be treated surgically. This includes patients who were diagnosed being healthy and patients who were diagnosed having mild head deformities due to positional plagiocephaly. Thus, the control model represents a mixed group of children and should be used with caution when generating healthy subjects.

Using PCA assumes that the training data follows a multivariate normal distribution. This assumption does not hold up for a head model which includes different pathology classes. With respect to the classification, PCA serves as a reparameterization and ultimately as a dimensionality reduction procedure. This seems to be one of the key elements of our classification approach. PCA is the de-facto standard method for PDM generation, although some authors have proposed some alternatives for specific cases. Probabilistic principal component analysis (PPCA) has been proposed for datasets with missing data or outliers [56], but has higher computational costs. As we have a regular mesh and have removed corrupt scans before establishing dense correspondence, we employed WPCA.

Many authors proposed modifications to further improve SSMs. With respect to template morphing, multiple correspondences can be taken into account [57]. Some possible improvements for the statistical modeling include the use of PPCA [56], reparameterization of training shapes [58], the use of part-based models [44], or combining multiple models [59, 60]. [61] presented Gaussian process morphable models, modeling deformations as Gaussian processes, which increases model flexibility by the use of prior models, combining kernels, and operating in the continuous domain. [19] made use of domain-specific Gaussian process shape deformations for model building. These methods might further improve our model.

5 Conclusion

We presented the first head model of craniosynostosis patients and made it publicly available. We included pathology specific submodels, ready-to-use sampled instances of each submodel, and a texture model. Our model performs similar to state-of-the-art head models with respect to morphing and model metrics and captures craniosynostosis-specific features. We showcased two original craniosynostosis-specific applications of our model. Second, we presented craniosynostosis classification pipeline using the parameter vector of an SSM. We achieved state-of-the-art results comparable to both CT data and photogrammetric scans and to the best of our knowledge, we tested it on the largest craniosynostosis-specific dataset to date.

Declaration of Competing Interest

The authors declare that they have no known competing financial interests or personal relationships that could have appeared to influence the work reported in this paper.

CRediT author statement

Matthias Schaufelberger: Conceptualization, Methodology, Software, Validation, Formal analysis, Investigation, Data curation, Writing - original draft, Visualization. **Reinald Peter Kühle:** Conceptualization, Methodology, Investigation, Resources, Data curation, Writing - review & editing. **Andreas Wachter:** Conceptualization, Methodology, Writing - Review & Editing. **Frederic Weichel:** Conceptualization, Investigation, Resources, Data curation. **Niclas Hagen:** Conceptualization, Resources, Data curation. **Friedemann Ringwald:** Resources, Data curation. **Urs Eisenmann:** Conceptualization, Methodology, Writing - review & editing, Supervision, Project administration, Funding acquisition. **Jürgen Hoffmann:** Resources, Supervision, Project administration, Funding acquisition. **Michael Engel:** Resources, Supervision, Project administration. **Christian Freudlsperger:** Conceptualization, Methodology, Investigation, Resources, Writing - review & editing, Supervision, Project administration, Funding acquisition. **Werner Nahm:** Conceptualization, Methodology, Investigation, Writing - review & editing, Supervision, Project administration, Funding acquisition.

Acknowledgments

This work received funding by the HEiKA research project grant HEiKA.19–17. The authors acknowledge the support by the state of Baden-Württemberg through bwHPC. The authors would like to thank the reviewers for their valuable comments to improve their work.

A Description of optimal step nonrigid iterative closest points (OS-N-ICP) methods

To be consistent with the notation in the original paper [43], we change notation. The n_p template points are expressed as $\mathbf{V} \in \mathbb{R}^{n_p \times 3}$.

The unknown affine transformations are defined as $\mathbf{X} \in \mathbb{R}^{4n_p \times 3}$. The full cost function can be expressed as $E(\mathbf{X}) = \alpha E_s(\mathbf{X}) + E_d(\mathbf{X}) + \beta E_l(\mathbf{X})$. The stiffness term $E_s(\mathbf{X})$ can be described as the Kronecker product \otimes of the mesh topology matrix $\mathbf{M} \in \mathbb{R}^{n_e \times n_p}$ with n_e denoting the number of edges and n_p the number of points. The weight matrix $\mathbf{G} \in \mathbb{R}^{4 \times 4} = \text{diag}(1, 1, 1, \gamma)$ between rotational and skew parts against translational parts [43]:

$$E_s(\mathbf{X}) = \|(\mathbf{M} \otimes \mathbf{G})\mathbf{X}\|_F^2. \quad (8)$$

\mathbf{M} describes the connections between neighboring vertices (we use the node-arc incidence matrix [62] in which for each edge r we set $\mathbf{M}(r, i) = -1$ and $\mathbf{M}(r, j) = 1$). The distance term $E_d(\mathbf{X})$ describes how close the displaced template vertices are to the target vertices and can be written as:

$$E_d(\mathbf{X}) = \|\mathbf{W}(\mathbf{D}\mathbf{X} - \mathbf{U})\|_F^2. \quad (9)$$

$\mathbf{W} \in \mathbb{R}^{n_p \times n_p}$ is a diagonal weighting matrix which allows assigning different weights to each transformation. The sparse displacement matrix $\mathbf{D} \in \mathbb{R}^{n_p \times 4n_p}$ is a diagonal matrix with the homogeneous points $v_i = [x_i, y_i, z_i, 1]^T$ as its diagonal elements mapping the homogeneous template points to the respective affine transforms. $\mathbf{U} \in \mathbb{R}^{n_p \times 3}$ denotes the found correspondences from the target points.

Finally, the landmark term $E_1(\mathbf{X})$ is similar to the distance term while only the landmark points are considered:

$$E_1(\mathbf{X}) = \|(\mathbf{D}_L \mathbf{X} - \mathbf{U}_L)\|_F^2. \quad (10)$$

The complete cost function for N-ICP-A can be written as:

$$E(\mathbf{X}) = \left\| \begin{bmatrix} \alpha \mathbf{M} \otimes \mathbf{G} \\ \mathbf{W} \mathbf{D} \\ \beta \mathbf{D}_L \end{bmatrix} \mathbf{X} - \begin{bmatrix} \mathbf{0} \\ \mathbf{W} \mathbf{U} \\ \mathbf{U}_L \end{bmatrix} \right\|_F^2 \quad (11)$$

For the translation-only variant N-ICP-T, the unknown transformations are defined as translations $\mathbf{X} \in \mathbb{R}^{n_p \times 3}$. The cost function is changed accordingly:

$$E(\mathbf{X}) = \left\| \begin{bmatrix} \alpha \mathbf{M} \\ \mathbf{W} \mathbf{I}_{n_p} \end{bmatrix} \mathbf{X} - \begin{bmatrix} \mathbf{0} \\ \mathbf{W}(\mathbf{U} - \mathbf{V}) \end{bmatrix} \right\|_F^2 \quad (12)$$

B Description of Laplace-Beltrami regularized projection methods

Laplace-Beltrami regularized projection (LBRP) [21, 34] relies on mutual correspondences between template and target and uses the Laplace-Beltrami (LB) operator $\mathbf{L}_0 \in \mathbb{R}^{n_p \times n_p}$ computed on the original template as a regularization, controlled by the stiffness parameter λ . A higher λ puts more weight to the LB term of the equation, leading to a mesh which retains its original shape. For a low λ , the original template shape is disregarded and is mapped closer to the target mesh, which might lead to irregularities in the projection. This template projection step can be described using [34, 21]:

$$\begin{bmatrix} \lambda \mathbf{L}_0 \\ \mathbf{S}_X \end{bmatrix} \mathbf{X} = \begin{bmatrix} \lambda \mathbf{L}_0 \mathbf{X}_0 \\ \mathbf{S}_Y \mathbf{Y} \end{bmatrix}, \quad (13)$$

The two Boolean selection matrices $\mathbf{S}_X \in [0, 1]^{k \times n_n}$ and $\mathbf{S}_Y \in [0, 1]^{k \times n_t}$ select the k correspondences on the template and target. n_p denotes the number of template points, n_t the number of target points.

For the 2S-LBRP, we essentially perform this template projection twice, first to adapt the template to the target and then refining it with decreased stiffness to let it deform more strongly to the target. This is a similar approach to the template adaption described in [34].

For the ICPD-LBRP [34], we first employ the adaptive template projection with a high λ , then alternate between the rigid coherent point drift (CPD) and nonrigid CPD [41] and conclude with the adaptive template projection with a small λ . For our dataset, this increased robustness compared to using the affine CPD variant as proposed in [34]. For further reading on the iterative coherent point drift and the template adaption of the LBRP, the reader is referred to [34].

C Evaluation of the morphing methods

We present mean and standard deviations for each error metric in Table 4. Cumulative errors for each metric show the distribution of each error and are displayed in Fig. 10. LBRP methods showed

smaller landmark errors and larger surface normal deviations compared to OS-N-ICP. N-ICP-A had the lowest vertex-to-nearest-neighbor distance errors. Surface normal deviations were for all methods larger than 17° .

Table 4: Mean error and standard deviation for each morphing method. Boldface shows smallest error for each metric.

Morphing method	Mean landmark error (mm)	Mean vertex-to-nearest-neighbor distance (mm)	Mean surface normals deviations (degree)
Nonrigid iterative closest points affine (N-ICP-A)	6.533 ± 1.796	0.007 ± 0.003	33.488 ± 1.578
Nonrigid iterative closest point translation (N-ICP-T)	5.699 ± 1.789	0.302 ± 0.01	23.242 ± 1.849
Two-step Laplace-Beltrami regularized projection (2S-LBRP)	4.185 ± 1.205	0.785 ± 0.17	20.392 ± 1.466
Iterative coherent point drift with Laplace-Beltrami regularized projection (ICPD-LBRP)	4.071 ± 1.163	0.272 ± 0.049	29.255 ± 2.12

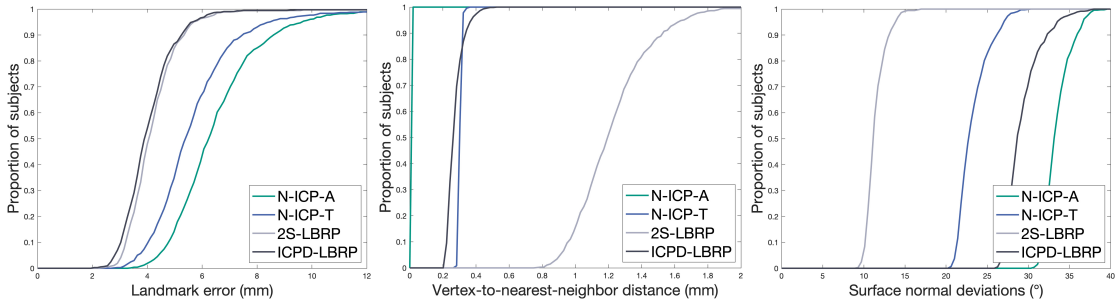


Figure 10: Proportion of subjects with mean landmark error, vertex-to-nearest-neighbor-distances, and surface normal. We compared nonrigid iterative closest points affine, nonrigid iterative closest point translation, two-step Laplace-Beltrami regularized projection (2S-LBRP), and iterative coherent point drift with Laplace-Beltrami regularized projection (ICPD-LBRP). The graph shows the proportion of subjects less than the abscissa value. Higher is better.

Fig. 11 shows the compactness of the SSM. The most compact models were produced by N-ICP-A and N-ICP-T, while generalization error and specificity error were larger (Fig. 12).

D Comparison of classification results for all four morphing methods

In Table 5 we show the classification results per morphing method and classification approach. LDA consistently yielded the highest accuracy regardless of the morphing method. Using LDA,

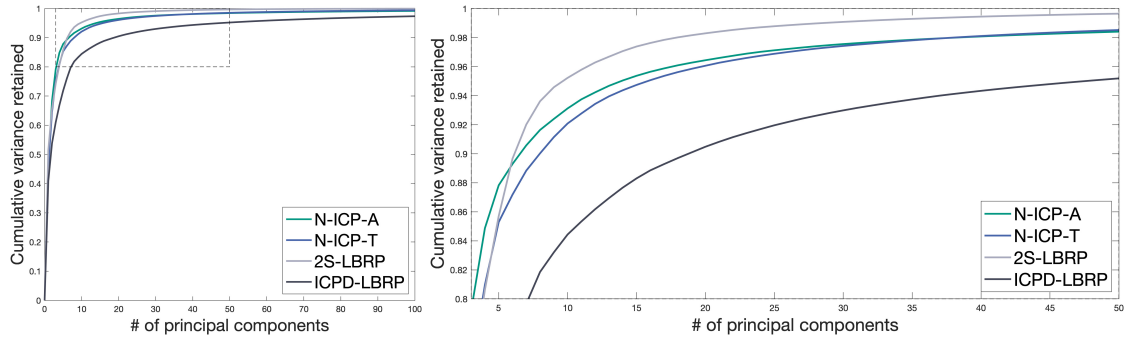


Figure 11: Compactness as a function of the number of principal components of the full shape model. We compared nonrigid iterative closest points affine (N-ICP-A), nonrigid iterative closest point translation (N-ICP-T), two-step Laplace-Beltrami regularized projection (2S-LBRP), and iterative coherent point drift with Laplace-Beltrami regularized projection (ICPD-LBRP). Left: full compactness, right: zoom-in. A higher value is better.

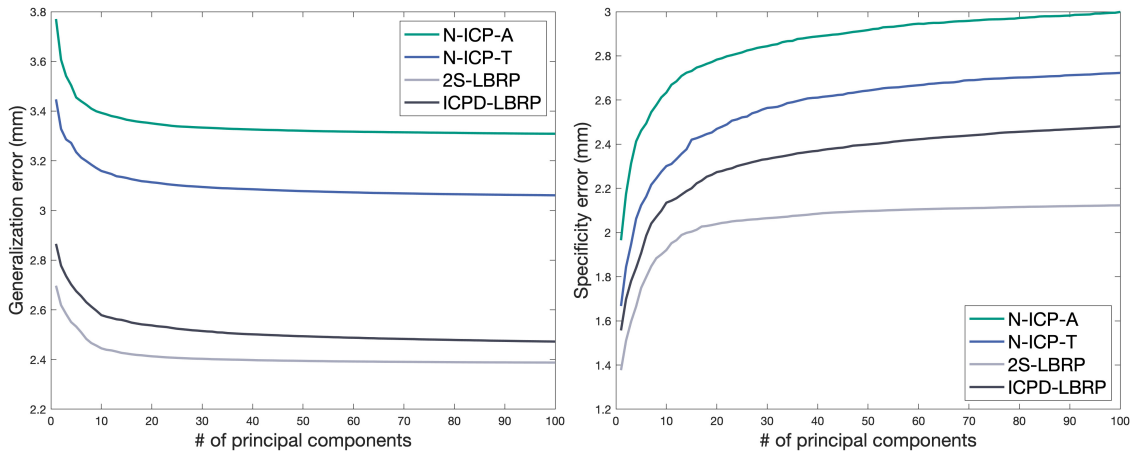


Figure 12: Generalization and specificity errors as functions of the number of principal components of the full shape model. We compared nonrigid iterative closest points affine (N-ICP-A), nonrigid iterative closest point translation (N-ICP-T), two-step Laplace-Beltrami regularized projection (2S-LBRP), and iterative coherent point drift with Laplace-Beltrami regularized projection (ICPD-LBRP). Left: generalization error, right: specificity error. For both metrics, a lower error is better.

all morphing methods obtained accuracies of 97.0% or higher. Note that N-ICP-T model scores the highest accuracy although it did not perform best in any of the evaluation criteria.

E Landmarks

Table 6 shows the landmarks annotated by the medical staff.

Table 5: Highest accuracy for each classifier and morphing methods. Optimal number of principal components is given in brackets. Underlined accuracy indicates optimal classifier per method and boldface optimal classifier overall.

Morphing method	LDA	SVM	NB	kNN	BDT
Nonrigid iterative closest points affine	<u>0.978</u> (44)	0.962 (46)	0.946 (23)	0.916 (23)	0.826 (22)
Nonrigid iterative closest point translation	0.981 (54)	0.959 (23)	0.946 (28)	0.910 (9)	0.842 (10)
Two-step Laplace-Beltrami regularized projection	<u>0.970</u> (50)	<u>0.970</u> (31)	0.959 (23)	0.946 (10)	0.861 (8)
Iterative coherent point drift with Laplace-Beltrami regularized projection	<u>0.975</u> (91)	0.962 (13)	0.951 (23)	0.951 (10)	0.847 (8)

Table 6: Landmarks on 3D surface scans provided by the medical staff. We use the cephalometric landmark notation of [63].

Landmark	Abbreviation
Tragion (left and right)	(t_l) and (t_r)
Sellion	(se)
Exocanthion (left and right)	(ex_l) and (ex_r)
Subnasale	(sn)
Labiale Superius	(ls)
Otobasion superius (left and right)	(obs_l) and (obs_r)
Soft tissue gnathion	(gn)

F Hyperparameters for template morphing

Table 7 lists the hyperparameters used in each method.

Table 7: Hyperparameters used for the template morphing approaches.

Two-step Laplace-Beltrami regularized projection (2S-LBRP) (notation of [34])	
Stiffness first morph	$\lambda_1 = 10$
Stiffness second morph	$\lambda_2 = 0.1$
Iterative coherent point drift with Laplace-Beltrami regularized projection (ICPD-LBRP) (notation of [34])	
Stiffness first morph	$\lambda_1 = 10$
Iterative coherent point drift (ICPD)-Loop	For each iteration, perform first <i>cpdRigid</i> , then <i>cpdNonrigid</i>
<i>cpdNonrigid</i> smoothing weight:	3
<i>cpdNonrigid</i> tolerance	$1 \cdot 10^{-5}$
Exit condition	fewer than 1% of nearest neighbors between iterations change
Stiffness second morph	$\lambda_2 = 0.1$ with Laplace matrix resulting from first morph
Nonrigid iterative closest points affine (N-ICP-A) and nonrigid iterative closest point translation (N-ICP-T) (notation of [43])	
Iterations	$n = 80$
Stiffness parameter α in iteration n	$\alpha_n = 10^8 \cdot 0.8^n$
Landmark weight in iteration n β	if $n < 51$ $\beta_n = 1$, else $\beta_n = 0$
Exit condition ϵ for each fixed stiffness α	$\epsilon < 100$
Valid normals for correspondence establishment φ	$\varphi < 45^\circ$
Rotation weight γ	$\gamma = 1$

References

- [1] Sheree L. Boulet, Sonja A. Rasmussen, and Margaret A. Honein. A population-based study of craniosynostosis in metropolitan Atlanta, 1989–2003. *American Journal of Medical Genetics Part A*, 146A(8):984–991, April 2008.
- [2] L.Ronald French, Ian T. Jackson, and L.Joseph Melton. A population-based study of craniosynostosis. *Journal of Clinical Epidemiology*, 43(1):69–73, January 1990.
- [3] Avinoam Shuper. The Incidence of Isolated Craniosynostosis in the Newborn Infant. *Archives of Pediatrics & Adolescent Medicine*, 139(1):85, January 1985.
- [4] Anna K Coussens, Christopher R Wilkinson, Ian P Hughes, C Phillip Morris, Angela van Daal, Peter J Anderson, and Barry C Powell. Unravelling the molecular control of calvarial suture fusion in children with craniosynostosis. *BMC Genomics*, 8(1):458, December 2007.
- [5] Dominique Renier, Christian Sainte-Rose, Daniel Marchac, and Jean-François Hirsch. Intracranial pressure in craniostenosis. *Journal of Neurosurgery*, 57(3):370–377, September 1982.
- [6] Kathleen A. Kapp-Simon, Matthew L. Speltz, Michael L. Cunningham, Pravin K. Patel, and Tadanori Tomita. Neurodevelopment of children with single suture craniosynostosis: A review. *Child’s Nervous System*, 23(3):269–281, January 2007.
- [7] Brendan F. Judy, Jordan W. Swanson, Wuyang Yang, Phillip B. Storm, Scott P. Bartlett, Jesse A. Taylor, Gregory G. Heuer, and Shih-Shan Lang. Intraoperative intracranial pressure monitoring in the pediatric craniosynostosis population. *Journal of Neurosurgery: Pediatrics*, 22(5):475–480, November 2018.
- [8] Michael Engel, Gregor Castrillon-Oberndorfer, Juergen Hoffmann, and Christian Freudlsperger. Value of preoperative imaging in the diagnostics of isolated metopic suture synostosis: A risk–benefit analysis. *Journal of Plastic, Reconstructive & Aesthetic Surgery*, 65(9):1246–1251, September 2012.
- [9] N. Bannink, E. Nout, E.B. Wolvius, H.L.J. Hoeve, K.F.M. Joosten, and I.M.J. Mathijssen. Obstructive sleep apnea in children with syndromic craniosynostosis: Long-term respiratory outcome of midface advancement. *International Journal of Oral and Maxillofacial Surgery*, 39(2):115–121, February 2010.
- [10] Jeffrey A. Fearon, Rachel A. Ruotolo, and John C. Kolar. Single Sutural Craniosynostoses: Surgical Outcomes and Long-Term Growth. *Plastic and Reconstructive Surgery*, 123(2):635–642, February 2009.
- [11] Christian Freudlsperger, Sahra Steinmacher, Daniel Saure, Jens P. Bodem, Reinald Kühle, Jürgen Hoffmann, and Michael Engel. Impact of severity and therapy onset on helmet therapy in positional plagiocephaly. *Journal of Cranio-Maxillofacial Surgery*, 44(2):110–115, February 2016.
- [12] S. Nagaraja, P. Anslow, and B. Winter. Craniosynostosis. *Clinical Radiology*, 68(3):284–292, March 2013.
- [13] John A. Persing, John A. Jane, and Mark Shaffrey. Virchow and the Pathogenesis of Craniosynostosis: A Translation of His Original Work. *Plastic and Reconstructive Surgery*, 83(4):738–742, April 1989.

- [14] Karen A. Eley, Stephen R. Watt-Smith, Fintan Sheerin, and Stephen J. Golding. “Black Bone” MRI: A potential alternative to CT with three-dimensional reconstruction of the craniofacial skeleton in the diagnosis of craniosynostosis. *European Radiology*, 24(10):2417–2426, October 2014.
- [15] Anne Saarikko, Eero Mellanen, Linda Kuusela, Junnu Leikola, Atte Karppinen, Taina Autti, Pekka Virtanen, and Nina Brandstack. Comparison of Black Bone MRI and 3D-CT in the preoperative evaluation of patients with craniosynostosis. *Journal of Plastic, Reconstructive & Aesthetic Surgery*, 73(4):723–731, April 2020.
- [16] Christian Mertens, Eline Wessel, Moritz Berger, Oliver Ristow, Jürgen Hoffmann, Katinka Kansy, Christian Freudlsperger, Heidrun Bächli, and Michael Engel. The value of three-dimensional photogrammetry in isolated sagittal synostosis: Impact of age and surgical technique on intracranial volume and cephalic index—a retrospective cohort study. *Journal of Cranio-Maxillofacial Surgery*, 45(12):2010–2016, December 2017.
- [17] T. F. Cootes, C. J. Taylor, D. H. Cooper, and J. Graham. Training Models of Shape from Sets of Examples. In David Hogg and Roger Boyle, editors, *BMVC92*, pages 9–18. Springer London, London, 1992.
- [18] Volker Blanz and Thomas Vetter. A morphable model for the synthesis of 3D faces. In *Proceedings of the 26th Annual Conference on Computer Graphics and Interactive Techniques - SIGGRAPH '99*, pages 187–194, Not Known, 1999. ACM Press.
- [19] Thomas Gerig, Andreas Morel-Forster, Clemens Blumer, Bernhard Egger, Marcel Lüthi, Sandro Schönborn, and Thomas Vetter. Morphable Face Models - An Open Framework. *arXiv:1709.08398 [cs]*, September 2017.
- [20] James Booth, Anastasios Roussos, Stefanos Zafeiriou, Allan Ponniah, and David Dunaway. A 3D Morphable Model Learnt from 10,000 Faces. In *2016 IEEE Conference on Computer Vision and Pattern Recognition (CVPR)*, pages 5543–5552, Las Vegas, NV, June 2016. IEEE.
- [21] Hang Dai, Nick Pears, and Christian Duncan. A 2D Morphable Model of Craniofacial Profile and Its Application to Craniosynostosis. In María Valdés Hernández and Víctor González-Castro, editors, *Medical Image Understanding and Analysis*, volume 723, pages 731–742. Springer International Publishing, Cham, 2017.
- [22] Bernhard Egger, William A. P. Smith, Ayush Tewari, Stefanie Wuhrer, Michael Zollhoefer, Thabo Beeler, Florian Bernard, Timo Bolkart, Adam Kortylewski, Sami Romdhani, Christian Theobalt, Volker Blanz, and Thomas Vetter. 3D Morphable Face Models—Past, Present, and Future. *ACM Transactions on Graphics*, 39(5):1–38, October 2020.
- [23] Anna Fabijańska and Tomasz Wegliński. The quantitative assessment of the pre- and postoperative craniosynostosis using the methods of image analysis. *Computerized Medical Imaging and Graphics*, 46:153–168, December 2015.
- [24] Alessandro Borghi, Naiara Rodriguez Florez, Federica Ruggiero, Greg James, Justine O’Hara, Juling Ong, Owase Jeelani, David Dunaway, and Silvia Schievano. A population-specific material model for sagittal craniosynostosis to predict surgical shape outcomes. *Biomechanics and Modeling in Mechanobiology*, 19(4):1319–1329, August 2020.

- [25] S. Ruiz-Correa, R.W. Sze, H.J. Lin, L.G. Shapiro, M.L. Speltz, and M.L. Cunningham. Classifying Craniosynostosis Deformations by Skull Shape Imaging. In *18th IEEE Symposium on Computer-Based Medical Systems (CBMS'05)*, pages 335–340, Dublin, Ireland, 2005. IEEE.
- [26] Jeffrey R. Marcus, Leahthan F. Domeshek, Andre M. Loyd, John M. Schoenleber, Rajesh R. Das, Roger W. Nightingale, and Srinivasan Mukundan. Use of a Three-Dimensional, Normative Database of Pediatric Craniofacial Morphology for Modern Anthropometric Analysis. *Plastic and Reconstructive Surgery*, 124(6):2076–2084, December 2009.
- [27] Carlos S. Mendoza, Nabile Safdar, Emmarie Myers, Tanakorn Kittisarapong, Gary F. Rogers, and Marius George Linguraru. Computer-Based Quantitative Assessment of Skull Morphology for Craniosynostosis. In David Hutchison, Takeo Kanade, Josef Kittler, Jon M. Kleinberg, Friedemann Mattern, John C. Mitchell, Moni Naor, Oscar Nierstrasz, C. Pandu Rangan, Bernhard Steffen, Madhu Sudan, Demetri Terzopoulos, Doug Tygar, Moshe Y. Vardi, Gerhard Weikum, Klaus Drechsler, Marius Erdt, Marius George Linguraru, Cristina Oyarzun Laura, Karun Sharma, Raj Shekhar, and Stefan Wesarg, editors, *Clinical Image-Based Procedures. From Planning to Intervention*, volume 7761, pages 98–105. Springer Berlin Heidelberg, Berlin, Heidelberg, 2013.
- [28] Carlos S. Mendoza, Nabile Safdar, Kazunori Okada, Emmarie Myers, Gary F. Rogers, and Marius George Linguraru. Personalized assessment of craniosynostosis via statistical shape modeling. *Medical Image Analysis*, 18(4):635–646, May 2014.
- [29] Hang Dai, Nick Pears, William Smith, and Christian Duncan. A 3D Morphable Model of Craniofacial Shape and Texture Variation. In *2017 IEEE International Conference on Computer Vision (ICCV)*, pages 3104–3112, Venice, October 2017. IEEE.
- [30] Naiara Rodriguez-Florez, Jan L. Bruse, Alessandro Borghi, Herman Vercruyse, Juling Ong, Greg James, Xavier Pennec, David J. Dunaway, N. U. Owase Jeelani, and Silvia Schievano. Statistical shape modelling to aid surgical planning: Associations between surgical parameters and head shapes following spring-assisted cranioplasty. *International Journal of Computer Assisted Radiology and Surgery*, 12(10):1739–1749, October 2017.
- [31] J.W. Meulstee, L.M. Verhamme, W.A. Borstlap, F. Van der Heijden, G.A. De Jong, T. Xi, S.J. Bergé, H. Delye, and T.J.J. Maal. A new method for three-dimensional evaluation of the cranial shape and the automatic identification of craniosynostosis using 3D stereophotogrammetry. *International Journal of Oral and Maxillofacial Surgery*, 46(7):819–826, July 2017.
- [32] Guido de Jong, Elmar Bijlsma, Jene Meulstee, Myrte Wennen, Erik van Lindert, Thomas Maal, René Aquarius, and Hans Delye. Combining deep learning with 3D stereophotogrammetry for craniosynostosis diagnosis. *Scientific Reports*, 10(1):15346, December 2020.
- [33] Pam Heutinck, Paul Knoops, Naiara Rodriguez Florez, Benedetta Biffi, William Breakey, Greg James, Maarten Koudstaal, Silvia Schievano, David Dunaway, Owase Jeelani, and Alessandro Borghi. Statistical shape modelling for the analysis of head shape variations. *Journal of Cranio-Maxillofacial Surgery*, 49(6):449–455, June 2021.
- [34] Hang Dai, Nick Pears, William Smith, and Christian Duncan. Statistical Modeling of Craniofacial Shape and Texture. *International Journal of Computer Vision*, 128(2):547–571, February 2020.

- [35] Thomas Albrecht, Reinhard Knothe, and Thomas Vetter. Modeling the remaining flexibility of partially fixed statistical shape models. In *in Proceedings of the Workshop on the Mathematical Foundations of Computational Anatomy*, 2008.
- [36] Jerry L. Hintze and Ray D. Nelson. Violin Plots: A Box Plot-Density Trace Synergism. *The American Statistician*, 52(2):181, May 1998.
- [37] Bastian Bechtold, Patrick Fletcher, Seamusholden, and Srinivas Gorur-Shandilya. Bastibe/Violinplot-Matlab: A Good Starting Point. Zenodo, February 2021.
- [38] Paolo Cignoni, Marco Callieri, Massimiliano Corsini, Matteo Dellepiane, Fabio Ganovelli, and Guido Ranzuglia. MeshLab: An Open-Source Mesh Processing Tool. *Eurographics Italian Chapter Conference*, page 8 pages, 2008.
- [39] Nico Pietroni, Marco Tarini, and Paolo Cignoni. Almost Isometric Mesh Parameterization through Abstract Domains. *IEEE Transactions on Visualization and Computer Graphics*, 16(4):621–635, July 2010.
- [40] P.J. Besl and Neil D. McKay. A method for registration of 3-D shapes. *IEEE Transactions on Pattern Analysis and Machine Intelligence*, 14(2):239–256, February 1992.
- [41] Andriy Myronenko and Xubo Song. Point Set Registration: Coherent Point Drift. *IEEE Transactions on Pattern Analysis and Machine Intelligence*, 32(12):2262–2275, December 2010.
- [42] Brett Allen, Brian Curless, and Zoran Popović. The space of human body shapes: Reconstruction and parameterization from range scans. *ACM Transactions on Graphics*, 22(3):587–594, July 2003.
- [43] Brian Amberg, Sami Romdhani, and Thomas Vetter. Optimal Step Nonrigid ICP Algorithms for Surface Registration. In *2007 IEEE Conference on Computer Vision and Pattern Recognition*, pages 1–8, Minneapolis, MN, USA, June 2007. IEEE.
- [44] Hang Dai, Nick Pears, and William Smith. Augmenting a 3D morphable model of the human head with high resolution ears. *Pattern Recognition Letters*, 128:378–384, December 2019.
- [45] Kai-kai Shen, Jurgen Fripp, Fabrice Mériaudeau, Gaël Chételat, Olivier Salvado, and Pierrick Bourgeat. Detecting global and local hippocampal shape changes in Alzheimer’s disease using statistical shape models. *NeuroImage*, 59(3):2155–2166, February 2012.
- [46] Corinna Cortes and Vladimir Vapnik. Support-vector networks. *Machine Learning*, 20(3):273–297, September 1995.
- [47] R. A. Fisher. The use of multiple measurements in taxonomic problems. *Annals of Eugenics*, 7(2):179–188, September 1936.
- [48] Harry Zhang. The optimality of naive bayes. volume 2, 01 2004.
- [49] A. D. Gordon, L. Breiman, J. H. Friedman, R. A. Olshen, and C. J. Stone. Classification and Regression Trees. *Biometrics*, 40(3):874, September 1984.
- [50] T. Cover and P. Hart. Nearest neighbor pattern classification. *IEEE Transactions on Information Theory*, 13(1):21–27, January 1967.

- [51] Fabian Pedregosa, Gaël Varoquaux, Alexandre Gramfort, Vincent Michel, Bertrand Thirion, Olivier Grisel, Mathieu Blondel, Peter Prettenhofer, Ron Weiss, Vincent Dubourg, Jake Vanderplas, Alexandre Passos, David Cournapeau, Matthieu Brucher, Matthieu Perrot, and Édouard Duchesnay. Scikit-learn: Machine learning in python. *J. Mach. Learn. Res.*, 12(null):2825–2830, nov 2011.
- [52] Martin A. Styner, Kumar T. Rajamani, Lutz-Peter Nolte, Gabriel Zsemlye, Gábor Székely, Christopher J. Taylor, and Rhodri H. Davies. Evaluation of 3D Correspondence Methods for Model Building. In Gerhard Goos, Juris Hartmanis, Jan van Leeuwen, Chris Taylor, and J. Alison Noble, editors, *Information Processing in Medical Imaging*, volume 2732, pages 63–75. Springer Berlin Heidelberg, Berlin, Heidelberg, 2003.
- [53] Rhodri Huw Davies. *Learning shape: optimal models for analysing natural variability*. PhD thesis, University of Manchester, 2002.
- [54] Thomas Albrecht, Marcel Lüthi, Thomas Gerig, and Thomas Vetter. Posterior shape models. *Medical Image Analysis*, 17(8):959–973, December 2013.
- [55] Hans Lamecker, Stefan Zachow, Hans-Christian Hege, M. Zöckler, and Ernst Haberl. Surgical treatment of craniosynostosis based on a statistical 3d-shape model: First clinical application. *International Journal of Computer Assisted Radiology and Surgery*, 1, 06 2006.
- [56] Marcel Lüthi, Thomas Albrecht, and Thomas Vetter. Building Shape Models from Lousy Data. In David Hutchison, Takeo Kanade, Josef Kittler, Jon M. Kleinberg, Friedemann Mattern, John C. Mitchell, Moni Naor, Oscar Nierstrasz, C. Pandu Rangan, Bernhard Steffen, Madhu Sudan, Demetri Terzopoulos, Doug Tygar, Moshe Y. Vardi, Gerhard Weikum, Guang-Zhong Yang, David Hawkes, Daniel Rueckert, Alison Noble, and Chris Taylor, editors, *Medical Image Computing and Computer-Assisted Intervention – MICCAI 2009*, volume 5762, pages 1–8. Springer Berlin Heidelberg, Berlin, Heidelberg, 2009.
- [57] Luming Liang, Mingqiang Wei, Andrzej Szymczak, Anthony Petrella, Haoran Xie, Jing Qin, Jun Wang, and Fu Lee Wang. Nonrigid iterative closest points for registration of 3D biomedical surfaces. *Optics and Lasers in Engineering*, 100:141–154, January 2018.
- [58] Rhodri H Davies, Carole J Twining, P Daniel Allen, Tim F Cootes, and Chris J Taylor. Building optimal 2D statistical shape models. *Image and Vision Computing*, 21(13-14):1171–1182, December 2003.
- [59] Stylianos Ploumpis, Haoyang Wang, Nick Pears, William A. P. Smith, and Stefanos Zafeiriou. Combining 3D Morphable Models: A Large Scale Face-And-Head Model. In *2019 IEEE/CVF Conference on Computer Vision and Pattern Recognition (CVPR)*, pages 10926–10935, Long Beach, CA, USA, June 2019. IEEE.
- [60] Stylianos Ploumpis, Evangelos Ververas, Eimear Oa Sullivan, Stylianos Moschoglou, Haoyang Wang, Nick Pears, William A. P. Smith, Baris Gecer, and Stefanos Zafeiriou. Towards a Complete 3D Morphable Model of the Human Head. *IEEE Transactions on Pattern Analysis and Machine Intelligence*, 43(11):4142–4160, November 2021.
- [61] Marcel Luthi, Thomas Gerig, Christoph Jud, and Thomas Vetter. Gaussian Process Morphable Models. *IEEE Transactions on Pattern Analysis and Machine Intelligence*, 40(8):1860–1873, August 2018.

- [62] Melvyn W. Jeter. *Mathematical Programming: An Introduction to Optimization*. Number 102 in Monographs and Textbooks in Pure and Applied Mathematics. M. Dekker, New York, 1986.
- [63] Gwen R.J. Swennen, Filip Schutyser, and Jarg-Erich Hausamen. *Three-Dimensional Cephalometry*. Springer Berlin Heidelberg, Berlin, Heidelberg, 2006.